Phytocarbon Dots as an Oral Nano-Degrader of ENO1 for Alleviating Hepatic Fibrosis

Lin Gao
Shandong First Medical University
Teng Liu
Shandong First Medical University
Yi-Kun Li
Shandong University
Ping Huang
Shandong First Medical University
Jing Li
Central Hospital of Zibo
Hong-Li Gao
Shandong First Medical University
Jing-Xin Li
Shandong University
Jun-Xia Zheng
Guangdong University of Technology
Zhi-Yuan Lu
luzhiyuan@sdfmu.edu.cn

Shandong First Medical University

Research Article

Keywords: Phytocarbon dots, Oral nano-degrader, Hepatic fibrosis, ENO1 degradation, PI3K/AKT pathway

Posted Date: July 3rd, 2026

DOI: https://doi.org/10.21203/rs.3.rs-10125058/v1

Additional Declarations: No competing interests reported.

Abstract

The lack of clinically effective targeted therapies for hepatic fibrosis presents a persistent challenge. In this study, we introduce an innovative oral nanotherapeutic platform based on phytocarbon dots derived from *Dianthus superbus* (D-CDs), which function as a target-specific protein degrader. D-CDs demonstrated potent anti-fibrotic efficacy in both toxin-induced and metabolic murine models of liver fibrosis with excellent biocompatibility. Mechanistically, we identified enolase 1 (ENO1) as the direct target. D-CDs do not inhibit ENO1 enzymatic activity but act as molecular glues that bind to an allosteric site, inducing a conformational change that licenses ubiquitination at K281 and triggers proteasomal degradation. This leads to sustained suppression of the PI3K/AKT-Smad3 pathway. This ENO1-dependent efficacy was validated through both genetic and pharmacological approaches, establishing a pioneering paradigm of oral nanomedicine for targeted degradation. Importantly, single-cell transcriptomic and histopathological analyses demonstrated that ENO1 is upregulated during hepatic stellate cell activation and overexpressed in human fibrotic livers, underscoring its clinical relevance. Collectively, our work presents not only a promising therapeutic candidate but also a versatile plant-based platform for degrading pathological proteins, with broad implications for the treatment of fibrosis and other protein-driven diseases.

Introduction

Hepatic fibrosis, characterized by excessive deposition of extracellular matrix (ECM), represents a common pathological outcome of chronic liver injury from diverse etiologies, including viral hepatitis, metabolic dysfunction, and toxins.[1, 2] This scarring process, driven primarily by the activation of hepatic stellate cells (HSCs), can progress to cirrhosis, liver failure, and hepatocellular carcinoma, posing a massive global health burden.[3, 4] Despite decades of research, no pharmacotherapy specifically designed to reverse or halt fibrosis has been approved for clinical use.[5] Current standard-of-care relies on the repurposing of non-specific agents, such as corticosteroids, N-acetylcysteine, or antivirals, which offer limited efficacy against fibrosis itself and are often plagued by significant off-target effects during long-term administration.[6–8] The urgent, unmet need for safe and effective anti-fibrotic agents underscores the necessity for novel therapeutic paradigms that move beyond symptom management to directly intercept core pathogenic mechanisms.

In recent years, carbon dots (CDs) have emerged as a promising class of nanomaterials for biomedical applications, prized for their excellent biocompatibility, ease of synthesis, and tunable physicochemical properties.[9] Notably, CDs derived from medicinal plants often exhibit intrinsic enzyme-mimetic activities, such as superoxide dismutase, peroxidase, and catalase-like functions. These activities enable CDs to modulate redox homeostasis, offering a “green” and potent platform for treating oxidative stress and inflammation-related diseases.[10–13] Despite these promising properties, the development of bioactive CDs as targeted, mechanism-based therapeutics has been hindered by a limited understanding of their specific interactions with cellular components.[14–16] In particular, how they engage with precise protein targets or influence downstream signaling pathways remains largely unclear.[17]

Although a limited number of recent studies have employed proteomic or interactome approaches to identify potential protein partners of functional CDs, the broader landscape of their biological interactions is still underexplored.[18, 19] Therefore, advancing CDs from mere antioxidant agents to mechanism-based precision medicines requires a paradigm shift: from observing phenotypic efficacy to elucidating precise target engagement and downstream signaling.

In this study, we report the discovery and mechanistic characterization of an orally active phytocarbon dot derived from *Dianthus superbus* (D-CDs), which functions as a target-specific protein degrader in hepatic fibrosis. We first observed that D-CDs potently attenuated HSC activation and fibrosis progression *in vitro* and *in vivo*, an effect not fully explained by general antioxidant activity. Through integrated proteomic screening and functional validation, we unexpectedly identified enolase 1 (ENO1), a glycolytic enzyme with emerging roles in fibrotic signaling, as the direct binding target of D-CDs. Importantly, D-CDs do not inhibit the enzymatic activity of ENO1. Instead, they act as molecular glues that bind to an allosteric site, inducing a conformational change that exposes lysine 281 and promotes its ubiquitination, leading to proteasomal degradation of ENO1 and sustained suppression of the downstream PI3K/AKT-Smad3 axis. To establish the clinical relevance of this target, we performed single-cell RNA-seq analysis of human fibrotic livers, which revealed a strong correlation between ENO1 expression and disease stage, and confirmed ENO1 protein overexpression in cirrhotic tissues by immunohistochemistry.

Collectively, this work moves beyond phenomenological description to establish a clear target-degradation mechanism for a plant-based nanomaterial (**Scheme 1**). We demonstrate that phytocarbon dots can be engineered as single-component, orally available “nano-degraders,” and validate ENO1 as a druggable node in hepatic fibrosis. These findings bridge herbal nanomedicine and targeted protein degradation, offering a new paradigm for the development of mechanism-driven, orally administered therapeutics against fibrosis and potentially other protein-driven diseases.

Scheme 1. Schematic illustration of the proposed mechanism by which oral D-CDs alleviate hepatic fibrosis. Orally administered D-CDs target and bind to enolase 1 (ENO1) on activated hepatic stellate cells (HSCs). This interaction promotes ENO1 ubiquitination and subsequent proteasomal degradation. Degradation of ENO1 inhibits the PI3K/AKT signaling pathway and its crosstalk with the TGF-β/Smad3 axis, leading to suppressed HSC activation, reduced extracellular matrix (ECM) deposition, and amelioration of hepatic fibrosis.

Materials and Methods

Materials and Reagents

The herbal material of *Dianthus superbus* (Qumai) was obtained from Bai Cao Tang (Beijing, China). Dialysis membrane tubing (molecular weight cut-off: 500 Da) was purchased from Beijing Ruida Henghui Technology. The EdU Cell Proliferation Kit with AF488 and ROS Assay Kit were purchased from Beyotime

Biotechnology (Shanghai, China). Detailed product information of chemicals and reagents used in this study is provided in Supplementary Table S1.

ITC experiments

ITC experiments were performed using a MicroCal PEAQ-ITC system (Malvern) at 25°C in PBS buffer (pH 7.4) [20]. Recombinant human ENO1 protein (5 μM) was placed in the sample cell, and D-CDs (1 mg/mL) were injected in 19 sequential injections of 2 μL each, with a stirring speed of 750 rpm. The reference power was set to 10 μcal/s. Data were analyzed using the MicroCal PEAQ-ITC Analysis software with a one-site binding model.

Molecular Docking and Molecular Dynamics Simulation

The crystal structure of the ENO1 protein was retrieved from the Protein Data Bank (PDB ID: 3B97). Carbon dots (CDs) were constructed and optimized using ChemOffice Suite. Semi-flexible docking between CDs and ENO1 was performed with AutoDock Vina (version 1.1.2). The complex system with the lowest binding energy and most rational binding mode was selected as the initial model for subsequent molecular dynamics (MD) simulations. MD simulations were conducted using the CUDA-accelerated AMBER20 pmemd engine (pmemd.cuda). RESP charges for CDs were generated using Multiwfn. The system was parameterized with the ff19SB protein force field, OPC water model, and GAFF2 ligand force field. Trajectory snapshots were saved at 100 ps intervals.

Single-cell analysis

Single-cell RNA-seq data from liver tissues of three patients with hepatic fibrosis and three healthy controls were processed using the Seurat R package (v4.0 or later). Cells expressing 200–2,000 genes with < 15% mitochondrial content were retained. Data were log-normalized, and highly variable genes were identified using the “vst” method, followed by scaling and PCA [21, 22]. Batch effects were corrected with Harmony using sample identity as the grouping variable. The top 15 Harmony dimensions were used for graph-based clustering (resolution 0.3) and UMAP visualization. Cell types were annotated using FindAllMarkers and canonical marker genes. ENO1 expression was visualized with FeaturePlot and VlnPlot, and cell-type proportions were compared using stacked bar plots. For pseudotime analysis, HSCs and ECM-HSCs were subsetted and analyzed with Slingshot using UMAP embeddings. Gene expression dynamics along pseudotime were assessed using GAM-based smoothing, revealing gradual upregulation of ENO1 during HSC-to-ECM-HSC differentiation. Default parameters were used unless otherwise specified.

Histological Evaluation

Following the establishment of the animal models, livers or other required organs were collected from the mice and fixed in 4% paraformaldehyde for 48 hours [23]. The fixed tissues were subsequently embedded in paraffin and sectioned into thin slices using a microtome. To comprehensively evaluate tissue morphology and pathological changes, multiple staining techniques were employed, including hematoxylin and eosin (H&E) for general histoarchitecture assessment, Masson's trichrome for collagen deposition and fibrosis visualization, Oil Red O for lipid accumulation analysis, and Sirius red for collagen fiber identification.

Mice

C57BL/6 mice (male, 8 weeks old) were supplied by Jinan Pengyue Experimental Animal (license No. 37072640101735252). All procedures involving animals were approved by the Animal Ethics Committee of Shandong First Medical University (No. W202410180680) and performed in compliance with institutional guidelines for the ethical use of laboratory animals.

For the CCl_4-induced hepatic fibrosis model, mice were randomly allocated to five groups (n = 8 per group): (1) naïve control, (2) CCl_4 model, (3) Silibinin (50 mg/kg, positive control), (4) D-CDs low-dose (5 mg/kg), and (5) D-CDs high-dose (15 mg/kg). Hepatic fibrosis was induced by intraperitoneal injection o 10 % CCl_4 solution in olive oil (v/v = 1:9, 6 mL/kg of body weight) twice weekly for eight weeks. Silibinin and D-CDs were administered orally every other day throughout the induction period. Control animals received equivalent volumes of olive oil and saline on the same schedule.

In the methionine/choline-deficient (MCD) diet-induced model, mice were fed an MCD diet for 6 weeks to induce hepatic fibrosis, while control mice received a methionine/choline-sufficient (MCS) diet. During the modeling period, MCD-fed mice were treated orally every other day with Silibinin (50 mg/kg) or D-CDs (5 or 15 mg/kg). Control mice received saline.

After the respective experimental durations (8 weeks for CCl_4 model, 6 weeks for MCD model), mice were euthanized under deep anesthesia. Blood samples were collected for serum biochemistry. Liver tissues were harvested and divided for histopathological analysis (H&E and Masson’s trichrome staining), RNA extraction (RT-qPCR), protein extraction (Western blot), and other molecular assays following established protocols.

Human Tissue Samples and Ethics Statement

Human liver tissue samples were obtained from patients with histopathologically confirmed hepatic fibrosis/cirrhosis as well as from control subjects with normal liver histology. All samples were collected with written informed consent from each participant and in strict accordance with the ethical guidelines approved by the Medical Ethics Committee of Zibo Central Hospital (Approval Number: 2026 YAN 025). Written informed consent was obtained from each participant prior to sample collection. Tissue

specimens were fixed in formalin, embedded in paraffin, and sectioned at 4 μm thickness for subsequent histological and immunohistochemical analyses.

Statistical analysis

All experiments were performed in triplicate. Data are presented as mean ± standard deviation (SD). Statistical analysis was conducted using an unpaired two-tailed Student's t-test.

For more experimental details, please refer to Supporting Information.

Results

Synthesis and Structural Characterization of D-CDs

D-CDs were prepared from *Dianthus superbus* via a one-pot hydrothermal method (**Fig. S1**), yielding a stable, dark-brown powder after dialysis and lyophilization. Transmission electron microscopy (TEM) was employed to elucidate the morphological characteristics of D-CDs. High-resolution TEM revealed well-defined lattice fringes with a spacing of 0.22 nm (Fig. 1a), corresponding to the (100) planes of graphitic carbon.[24] The images showed monodisperse, quasi-spherical nanoparticles with an average diameter of 2.23 ± 0.2 nm (Fig. 1b). Under 365 nm UV excitation, the aqueous dispersion of D-CDs exhibited strong blue photoluminescence and a distinct Tyndall effect (right inset of Fig. 1a), indicating excellent colloidal stability. Complementary X-ray diffraction (XRD) analysis further supported the amorphous carbon structure, showing a broad peak centered at approximately 22° (2θ) (Fig. 1c). Photoluminescence characterization highlighted the bioimaging potential of D-CDs, with excitation and emission maxima at 450 nm and 550 nm (red/blue curves, Fig. 1d), along with a characteristic UV–vis absorption band at 290 nm (black curve) associated with π − π* transitions. Environmental stability tests showed that the fluorescence intensity remained at95 % of the initial value after 16 days under ambient conditions (**Fig. S2**). The nanoparticles also withstood extreme pH values (3 − 10) and high ionic strength (1.0 M NaCl) (Fig. S2), demonstrating exceptional robustness.

X-ray photoelectron spectroscopy analysis confirmed the elemental composition of D-CDs as carbon (68.68%), nitrogen (6.00%), and oxygen (25.32%) (Fig. 1e). High-resolution C 1s spectra (Fig. 1f) identified three distinct carbon species: C − C/C = C (284.2 eV), C − O (287.0 eV), and C = O (288.4 eV). O 1s spectra (Fig. 1g) were dominated by contributions from C = O (531.5 eV) and C − O (532.6 eV). The deconvolution of the N 1s spectrum resolved two predominant peaks at binding energies of 399.7 and 401.5 eV, corresponding to pyrrolic N and graphitic N, respectively (Fig. 1h). Comparative FTIR spectroscopy revealed abundant surface functional groups on D-CDs (Fig. 1i), including O − H or N − H (3380 cm^{-1}), C − H (2952 cm^{-1}), C = O (1642 cm^{-1}), C = C (1411 cm^{-1}), and C − O (1077 cm^{-1}) stretching vibrations, indicating the presence of hydrophilic groups such as hydroxyl and amino groups. Structural characterization of D-CDs was further conducted using nuclear magnetic resonance (NMR) spectroscopy. The ^{1}H-NMR spectrum (Fig. 1j) revealed characteristic signals in the aromatic region, with

resonances between 6 and 10 ppm, which are attributable to aromatic hydrogen atoms. A signal at approximately 8.0 ppm indicated the presence of phenolic hydroxyl (– OH) groups, which are pharmacologically relevant due to their potent antioxidant activity through scavenging reactive oxygen species (ROS).[25] Complementary ^{13}C-NMR signals (**Fig. S3**) in the range of 20 – 100 ppm were assigned to aliphatic sp^3-hybridized C – O environments, confirming the existence of oxygen-rich functional groups on the CD surface. Signals in the 110 – 150 ppm region corresponded to sp^2-hybridized carbon atoms within aromatic frameworks, corroborating the aromatic nature of the carbon core. Additional signals (2.5–5 ppm) were ascribed to functional groups such as CH – N, N – H, and O – H, which contribute to surface passivation, hydrophilicity, and biocompatibility.

In summary, comprehensive characterization encompassing morphology, optical properties, environmental stability, surface chemistry, and molecular structure demonstrates that D-CDs possess a well-defined quasi-spherical nanostructure, establishing them as a promising theranostic platform for targeted biomedical applications.

D-CDs Attenuate HSC Activation and Fibrogenesis in vitro

The activation of hepatic stellate cells (HSCs) is a pivotal event in hepatic fibrosis, as these cells serve as the principal effectors driving excessive extracellular matrix (ECM) deposition.[26] This activation process is potently induced by the key profibrotic cytokine, transforming growth factor-β (TGF-β).[27] To evaluate the anti-fibrotic potential of D-CDs, we established an *in vitro* model by stimulating LX-2 cells with TGF-β in the presence of varying concentrations of D-CDs. Bright-field microscopy showed that D-CDs treatment markedly attenuated the TGF-β-induced morphological transition of LX-2 cells toward a myofibroblast-like phenotype (Fig. 2a, 2b). Furthermore, 5-ethynyl-2'-deoxyuridine (EdU) incorporation assays indicated that TGF-β stimulation significantly enhanced LX-2 cell proliferation, whereas D-CDs treatment effectively suppressed this effect (Fig. 2c, 2d). Consistent with these observations, CCK-8 assays confirmed that D-CDs inhibited cell proliferation in a dose-dependent manner (Fig. 2e).

We next examined how D-CDs influence the expression of key fibrotic markers. Using quantitative real-time PCR (RT-qPCR), we found that D-CDs treatment significantly downregulated the mRNA levels of *Acta2* and *Col1a1*, which encode α-smooth muscle actin and type I collagen, respectively, compared to the TGF-β-stimulated group (Fig. 2f, 2g). Consistently, western blot analysis further demonstrated that D-CDs substantially reduced the protein abundance of both α-SMA and Collagen 1 (Fig. 2h-j). Immunofluorescence staining clearly showed that the strong α-SMA signal induced by TGF-β was dramatically diminished following D-CDs intervention (Fig. 2k, 2l). Collectively, these results demonstrated that D-CDs exert potent anti-fibrotic effects by concurrently suppressing the expression of critical profibrotic genes and proteins, thereby mitigating the transition of fibroblasts into an activated myofibroblast phenotype.

Oxidative stress is a well-established driver of hepatic stellate cell (HSC) activation and a key contributor to hepatic fibrosis.[28] We therefore investigated whether the anti-fibrotic activity of D-CDs involves the mitigation of this pathway. Structurally, D-CDs are rich in surface phenolic hydroxyl and unsaturated

carbonyl groups, motifs commonly associated with radical-scavenging potential.[29] To systematically evaluate their intrinsic antioxidant properties, we performed a series of complementary in vitro assays. First, the total antioxidant capacity was measured using the $ABTS^{+}$ radical-cation decolorization assay, in which D-CDs exhibited potent, dose-dependent scavenging activity (**Fig. S4**). Second, the ability of D-CDs to neutralize superoxide anion ($O_2^{\bullet-}$) was evaluated using both the nitroblue tetrazolium (NBT) reduction method and the WST-1-based SOD activity assay, which together confirmed their concentration-dependent $O_2^{\bullet-}$ scavenging efficacy and significant SOD-mimetic capacity (**Fig. S5**). Finally, the hydroxyl radical ($^{\bullet}OH$) elimination efficiency was examined in a Fenton reaction system, where D-CDs also displayed pronounced scavenging activity (**Fig. S6**). Together, these results demonstrate that D-CDs possess broad-spectrum and potent antioxidant activity across multiple radical species.

We next asked whether this *in vitro* antioxidant profile translates to a cellular context. In TGF-β-stimulated LX-2 cells, D-CDs treatment significantly attenuated the accumulation of intracellular reactive oxygen species (ROS), as evidenced by a marked reduction in DCFH-DA fluorescence intensity (Fig. 2m, 2n). Collectively, these data establish that D-CDs can mitigate oxidative stress both directly in chemical assays and within activated HSCs. Nevertheless, given that the suppression of HSC activation by D-CDs was particularly potent and direct, we further hypothesized that a more specific, target-driven mechanism, beyond general redox modulation, likely underlies their primary anti-fibrotic efficacy.

D-CDs Alleviate Liver Fibrosis by Inhibiting the PI3K/AKT Signaling Pathway

To elucidate the molecular mechanism by which D-CDs against fibrosis, we performed transcriptomic profiling of TGF-β-activated LX-2 cells treated with or without D-CDs. Principal component analysis showed clear separation between groups, indicating a distinct transcriptional response induced by D-CDs (Fig. 3a). Differential expression analysis identified 2195 significantly altered genes (1395 up, 796 down), suggesting broad regulatory effects (Fig. 3b). To interpret the functional implications of these gene expression changes, we performed bioinformatic analysis. Gene Ontology enrichment analysis indicated that these differentially expressed genes were strongly associated with key fibrosis-related processes, including positive regulation of cell migration, oxidative stress response, and extracellular matrix organization (Fig. 3c and **Fig. S7**, **S8**). A heatmap was generated to depict the expression profiles of the significantly enriched genes involved in liver fibrosis-related pathways, revealing distinct clustering among the treatment groups. A heatmap of fibrosis-related genes confirmed that D-CDs broadly down-regulated pro-fibrotic transcripts (Fig. 3d). Further KEGG pathway analysis revealed that the PI3K/AKT signaling pathway was the most significantly enriched among the altered pathways (Fig. 3e), highlighting its central role in mediating the anti-fibrotic effects of D-CDs. We next validated the suppression of this pathway through multi-level experiments. Gene set enrichment analysis (GSEA) further demonstrated significant inhibition of PI3K/AKT signaling activity upon D-CDs treatment (Fig. 3f).

Based on these findings, we validated the mechanism at the protein level. Western blot analysis demonstrated that D-CDs effectively suppressed TGF-β-induced phosphorylation of PI3K and AKT (Fig. 3g, 3h). Consistent with prior reports that the PI3K/AKT pathway enhances Smad3-mediated fibrogenic responses,[30] the inhibition of PI3K/AKT led to a marked reduction in Smad3 phosphorylation (Fig. 3g), identifying Smad3 as a key downstream effector protein in this regulatory axis. qPCR analysis confirmed that D-CDs significantly downregulated the mRNA levels of four key fibrogenic genes downstream of the PI3K/AKT–Smad3 axis (*Fn1*, *Pdgfb*, *Egr1* and *Ccnd1*), further supporting the functional inhibition of this signaling pathway (Fig. 3i-l). Together, these results establish that inhibition of the PI3K/AKT signaling pathway, accompanied by downregulation of its downstream effector Smad3, constitutes a primary mechanism through which D-CDs exert their potent anti-fibrotic effects.

D-CDs Bind to and Promote Ubiquitin-Mediated Degradation of ENO1

To elucidate how D-CDs suppress the PI3K/AKT signaling pathway, we first sought to identify their direct molecular target. Integrated proteomic profiling of activated LX-2 cells revealed enolase 1 (ENO1) as a high-affinity binding candidate of D-CDs (Fig. 4a, 4b). Although traditionally known as a glycolytic enzyme, ENO1 also acts as a surface plasminogen receptor implicated in extracellular matrix remodeling and has been linked to fibrotic progression in other organs via the PI3K-AKT axis.[31, 32] Using cellular thermal shift assay (CETSA), we validated direct physical binding between D-CDs and ENO1, evidenced by thermal stabilization of the protein (Fig. 4c, 4d). Isothermal titration calorimetry (ITC) also confirmed direct binding between D-CDs and ENO1, with an apparent molar dissociation constant (Kd) of approximately 8 nM (Fig. 4e). The exothermic binding ($\Delta H = -8.312$ kJ/g) and positive entropy change ($\Delta S = 60.45$ J/g·K) indicate a thermodynamically favorable, multivalent interaction. We next assessed whether this binding affects the enzymatic activity of ENO1. Surprisingly, *in vitro* enzyme activity assays revealed that binding of D-CDs did not significantly alter the glycolytic function of ENO1 (**Fig. S9**). This finding prompted us to investigate further: if D-CDs do not act by inhibiting enzymatic activity, does this specific binding affect the stability of the ENO1 protein itself?

We therefore next examined whether D-CDs induce degradation of the target protein. Immunofluorescence staining showed that D-CDs treatment dose-dependently reduced ENO1 protein levels in LX-2 cells (Fig. 4f, g), which was further confirmed by western blot analysis (Fig. 4h, S10). Time-course analysis revealed rapid degradation, with ∼5 % reduction within 6 h (Fig. 4i, S11). Since the ubiquitin-proteasome system is a primary regulatory pathway for controlling intracellular ENO1 abundance,[33] we investigated whether D-CDs promote ENO1 degradation through this mechanism. Co-treatment with the proteasome inhibitor MG132 significantly rescued ENO1 protein levels following D-CDs treatment (Fig. 4j, S12), confirming proteasome-dependent degradation. Consistent with this, immunoprecipitation followed by anti-ubiquitin immunoblotting revealed a markedly stronger poly-ubiquitin laddering signal in D-CD-treated samples (Fig. 4k), providing direct evidence that D-CDs promote ENO1 ubiquitination.

To further elucidate the structural mechanism underlying D-CDs-induced ubiquitination, we performed all-atom molecular dynamics (MD) simulations. The systems reached equilibrium after 100 ns, and the stable trajectory (150–200 ns) was used for analysis (**Fig. S13**). The simulations revealed that D-CDs stably bind to a surface cavity on ENO1 distant from its catalytic center (Fig. 4l), which aligns with our observation that D-CDs do not inhibit ENO1 enzymatic activity. The binding was stabilized by hydrogen bonds between charged groups on D-CDs and ENO1 residues D238, K285, D286, Y287, G312, R426, and R429, as well as by hydrophobic interactions between the nitrogen-containing carbon skeleton of D-CDs and residues V173, V241, I284, P288, V289, V290, and I313 (Fig. 4k). Notably, D-CDs binding induces a local conformational rearrangement in ENO1, increasing the distance and inter-helical angle between α-helix 7 and α-helix 8 (Fig. 4m). This change disrupts the packing between K281 and S310, leading to enhanced solvent exposure of K281 (Fig. 4n). As K281 is a predicted ubiquitination site, its increased accessibility provides a structural mechanism for the enhanced ubiquitination of ENO1 observed in cells. In summary, these simulations demonstrate that D-CDs act as an allosteric modulator, binding remotely from the active site to selectively expose the ubiquitination site K281, thereby promoting ENO1 ubiquitination and subsequent degradation (Fig. 4o).

The Anti-fibrotic Efficacy of D-CDs is ENO1-Dependent

To establish whether the anti-fibrotic effects of D-CDs are mediated specifically through ENO1, we performed both genetic loss-of-function and pharmacological competition experiments. First, we used siRNA to genetically deplete ENO1 in LX-2 cells. Successful knockdown was confirmed by western blot (**Fig. S14**). Notably, loss of ENO1 potently suppressed the TGF-β-induced phosphorylation of key signaling nodes in the PI3K/AKT-Smad cascade (p-PI3K, p-AKT, and p-Smad3) and concurrently downregulated the expression of the fibrosis effector proteins α-SMA and collagen I (Fig. 5a, b). Consistent with these protein-level changes, qPCR analysis confirmed a significant reduction in the mRNA levels of *Acta2* and *Col1a1* (Fig. 5c). This genetic phenocopy of D-CDs treatment strongly suggested that ENO1 is a critical upstream regulator of the fibrotic signaling network in HSCs.

To further interrogate whether D-CDs require direct interaction with ENO1 to exert their effects, we employed the competitive inhibitor cinnamaldehyde (CA).[34] Co-treatment with CA effectively blocked the D-CDs-mediated reduction of ENO1 protein and restored the activity of the downstream PI3K/AKT pathway, as evidenced by recovered levels of p-PI3K and p-AKT (Fig. 5d, e and S15). Concordantly, the suppressive effect of D-CDs on the transcription of *Acta2* and *Col1a1* was also reversed in the presence of CA (Fig. 5f). This pharmacological rescue experiment provided direct evidence that the anti-fibrotic activity of D-CDs is contingent upon their specific binding to ENO1. Finally, to assess the functional consequence of ENO1 loss on a key pro-fibrotic phenotype, we evaluated HSC proliferation. EdU incorporation assays revealed that siRNA-mediated knockdown of ENO1 significantly inhibited TGF-β-driven proliferation of LX-2 cells (Fig. 5g, h), mirroring the anti-proliferative effect of D-CDs treatment.

In summary, the convergence of genetic knockdown and pharmacological inhibition data unequivocally demonstrates that ENO1 is a master regulatory node in HSC activation and that the therapeutic efficacy of D-CDs is mechanistically rooted in their targeted engagement and functional perturbation of ENO1.

Single-Cell and Human Tissue Validation of ENO1 in Hepatic Fibrosis

To definitively establish ENO1 as a clinically relevant target, we interrogated its expression dynamics across the spectrum of human hepatic fibrosis by integrating single-cell transcriptomics with histopathological validation. First, we analyzed single-cell RNA-sequencing (scRNA-seq) data from liver tissues of three patients with hepatic fibrosis (GSE210077).[35] Unsupervised clustering and uniform manifold approximation and projection (UMAP) visualizations identified ten major cell populations, which were annotated based on established marker genes (Fig. 6a and S16). These included hepatocyte subclasses, hepatic stellate cells (HSCs), endothelial cells, cholangiocytes, and immune subsets. Notably, ENO1 expression was predominantly enriched in fibrosis-associated cell types, particularly in ECM HSCs and two distinct fibrotic hepatocyte subsets (Fibrotic Hep1 and Fibrotic Hep2) (Fig. 6b). Consistent with this expression pattern, cellular proportion analysis revealed a marked expansion of these ENO1-high populations in fibrotic livers compared to healthy controls (Fig. 6c and S16). At the tissue level, violin plot analysis further confirmed a significant upregulation of overall ENO1 expression in fibrotic samples (Fig. 6d).

Given the pronounced ENO1 expression in ECM HSCs, we next sought to characterize its dynamic regulation during HSC activation. Pseudotime trajectory inference using Slingshot reconstructed a continuous differentiation path from quiescent HSCs toward activated, ECM HSCs (Fig. 6e). Along this activation trajectory, ENO1 expression progressively increased with advancing pseudotime (Fig. 6f), suggesting its potential role in promoting HSC activation and extracellular matrix remodeling during fibrogenesis.

We further validated the pathological relevance of ENO1 through direct histopathological examination of human liver specimens. Hematoxylin and eosin (H&E) and Masson’s trichrome staining of cirrhotic tissues confirmed severe architectural distortion, inflammatory infiltration, and extensive collagen deposition, consistent with advanced fibrosis (Fig. 6g, h). Immunohistochemical analysis demonstrated markedly intensified ENO1 protein expression in cirrhotic livers compared to controls, with strong signals localized to regions of active fibrogenesis (Fig. 6i). Semiquantitative scoring confirmed a significant increase in ENO1 immunoreactivity in fibrotic tissues (**Fig. S17**).

In summary, by combining single-cell transcriptomics with human tissue pathology, we establish ENO1 as a fibrosis-associated protein that is upregulated during HSC activation and consistently overexpressed in human cirrhotic livers, thereby reinforcing its potential as a therapeutic target for hepatic fibrosis.

D-CDs Ameliorate CCL_4 Induced Mouse Liver Fibrosis by Targeting the ENO1-PI3K/AKT Axis

Having established the anti-fibrotic mechanism of D-CDs *in vitro*, we next evaluated their therapeutic efficacy in a well-characterized CCl_4-induced murine model of hepatic fibrosis.[36] As illustrated in Fig. 7a, mice received oral administration of D-CDs at two doses (5 or 15 mg/kg) or Silibinin (50 mg/kg, positive control) during the 8-week fibrosis induction period. The experimental groups are detailed in Fig. 7b. D-CDs treatment, particularly at the higher dose, alleviated the CCl_4-induced body weight loss (Fig. 7c) and significantly attenuated liver injury, as reflected by reduced serum levels of aspartate aminotransferase (AST), alanine aminotransferase (ALT), and alkaline phosphatase (ALP) (Fig. 7d-f). Macroscopic inspection of livers revealed that D-CDs markedly diminished the fibrotic nodules present in the CCl_4 model group (Fig. 7g). Histopathological analysis provided further evidence of protection. H&E staining revealed that D-CDs alleviated architectural distortion, hepatocyte ballooning, necrosis, and inflammatory infiltration (Fig. 7h). Sirius Red and Masson's trichrome staining confirmed that D-CDs potently reduced collagen deposition and fibrotic septa formation, with the high-dose group exhibiting efficacy superior to that of Silibinin (Fig. 7h).

To determine whether the mechanism identified *in vitro* operates *in vivo*, we analyzed key molecular markers in liver tissues. RT-qPCR and western blot analyses consistently showed that D-CDs significantly suppressed the up-regulation of α-SMA and Collagen 1 induced by CCl_4 (Fig. 7i-m). Furthermore, D-CDs treatment downregulated the mRNA expression of the hepatic stellate cell activation markers Vimentin and Desmin compared with the model group (**Fig. S18**). Crucially, western blotting confirmed that D-CDs down-regulated ENO1 protein levels and concurrently inhibited the phosphorylation of PI3K, AKT, and Smad3 in fibrotic livers (Fig. 7k, S19). Collectively, these *in vivo* results demonstrate that oral administration of D-CDs effectively attenuates established hepatic fibrosis by specifically targeting the ENO1–PI3K/AKT–Smad3 axis in the liver, thereby validating our mechanistic model in a whole-organism context.

D-CDs Alleviate MCD Diet-Induced Metabolic-Associated Liver Fibrosis via the ENO1-PI3K/AKT Axis

To substantiate the broad therapeutic potential of D-CDs across different fibrotic etiologies, we evaluated their efficacy in a methionine-choline-deficient (MCD) diet-induced mouse model,[37] which recapitulates key aspects of metabolic dysfunction-associated steatohepatitis (MASH) and fibrosis. After 1 week of MCD diet-induced injury, mice received daily oral administration of D-CDs (5 or 15 mg/kg) or Silibinin for 8 weeks (Fig. 8a). D-CDs treatment significantly alleviated MCD-diet-induced hepatomegaly, as indicated by improved body weight and liver-to-body weight ratios (Fig. 8c). Consistent with this phenotypic improvement, serum levels of liver injury markers, including ALT, AST, and ALP (Fig. 8d-f), were markedly reduced by D-CDs treatment, with the high dose showing particularly potent activity. Macroscopic evaluation further revealed that D-CDs diminished the fibrotic nodularity on the

liver surface observed in the MCD model group (Fig. 8g). Histological analysis provided multi-faceted evidence of protection. H&E staining indicated attenuated inflammatory infiltration, and Masson's trichrome staining confirmed a pronounced reduction in collagen deposition (Fig. 8h). Importantly, Oil Red O staining demonstrated that D-CDs also suppressed hepatic lipid accumulation (Fig. 8h), indicating a beneficial effect on the steatotic component of MASH.

At the molecular level, D-CDs treatment dose-dependently down-regulated the mRNA and protein expression of the fibrotic markers α-SMA and Collagen 1 (Fig. 8i-m). Consistent with this anti-fibrotic effect, the treatment also significantly reduced the gene expression of stellate cell activation markers Vimentin and Desmin (**Fig. S20**). Most notably, and in direct alignment with the mechanism established *in vitro* and in the CCl_4 model, D-CDs reduced hepatic ENO1 protein levels and inhibited phosphorylation of PI3K, AKT, and Smad3 (Fig. 8k, S21). Together, these results demonstrate that D-CDs effectively ameliorate metabolically driven hepatic fibrosis through consistent suppression of the ENO1–PI3K/AKT–Smad3 axis across both toxic and dietary fibrotic models.

Comprehensive Biosafety and Biodistribution Profiling of D-CDs

Prior to considering the therapeutic application of any nanomaterial, a systematic evaluation of its biosafety is paramount. To this end, we conducted a multi-tiered toxicological assessment of D-CDs. The initial in vitro safety profile was established using three human normal cell lines representing potential exposure or metabolic routes, including AML-12, HUVEC, and NCM460 cells. After 24 h of exposure, CCK-8 assays showed that cell viability remained above 98% even at the highest concentration of D-CDs tested (Fig. 9a, b and S22), indicating minimal cytotoxicity. We then assessed developmental and systemic toxicity *in vivo*. In zebrafish embryos, exposure to D-CDs did not induce significant morphological abnormalities in the yolk sac, nor did it adversely affect hatching rates (48 and 92 h) or 96-h survival rates (Fig. 9c, 9d and S23). Hemocompatibility was confirmed by a hemolysis assay, which showed no significant red blood cell lysis at any tested concentration of D-CDs (Fig. 9e).

To evaluate subchronic oral toxicity, mice were administered D-CDs daily at high doses (100 or 500 mg/kg) for 4 weeks. One month after the initiation of dosing, comprehensive key serum biochemical markers (Fig. 9f, 9g and S24) and hematological parameters (**Fig. S25**) all remained within normal physiological ranges. Subsequent histopathological examination of major organs (heart, liver, spleen, lungs, and kidneys) revealed no notable lesions or abnormalities in H&E-stained sections (Fig. 9h). Finally, we investigated the *in vivo* distribution of D-CDs using Cy5-labeled nanoparticles. After intravenous injection, fluorescence signals were detected in multiple tissues, peaking at 3 h and being largely cleared by 48 h, indicating efficient clearance of D-CDs (Fig. 9i, S26). The strongest signals were localized predominantly in the kidneys and liver, aligning with the primary routes of metabolism and excretion.[38] In summary, these findings robustly support the further biomedical development and translational potential of D-CDs as a safe nano-therapeutic agent.

Discussion

Despite advances in understanding hepatic fibrosis, the absence of clinically approved targeted therapies remains a major translational gap.[39] Here, we bridge this gap by transforming a traditional herbal medicine into an orally active nanotherapeutic with a defined protein-degradation mechanism. Specifically, we engineered phytocarbon dots (D-CDs) from *Dianthus superbus* that function as a first-in-class oral nano-degrader, directly targeting enolase 1 (ENO1) for ubiquitin-proteasomal destruction, thereby suppressing the PI3K/AKT-Smad3 axis and attenuating fibrosis. This work provides a conceptual and practical advance by integrating herbal nanomedicine with the targeted protein degradation paradigm.

While proteolysis-targeting chimeras (PROTACs) have established a powerful paradigm for degrading disease-driving proteins, their clinical translation is often constrained by poor oral bioavailability and complex synthesis.[40] Nanoparticle-based systems offer an alternative route, yet many require intravenous administration and lack the inherent safety of natural products.[41] Here, we show that carbon dots synthesized from a herb traditionally used for liver disorders, can be designed as a single-component, orally administered nano-degrader. D-CDs combine the favorable safety profile of their botanical origin with effective systemic exposure and liver accumulation after oral delivery, addressing a key limitation of current degrader modalities and providing a scalable, plant-inspired therapeutic platform.

A major barrier in developing bioactive nanomaterials is the frequent absence of well-defined molecular targets. Using integrated proteomic and transcriptomic analysis, we identified enolase 1 (ENO1) as the direct target of D-CDs. Beyond its role in glycolysis, ENO1 serves as a surface plasminogen receptor implicated in extracellular matrix remodeling and fibrogenic signaling.[42] Its pathological relevance is underscored by significant upregulation in human fibrotic liver samples. Direct binding between D-CDs and ENO1 was confirmed via cellular thermal shift assays and competitively inhibited by cinnamaldehyde. To our knowledge, this is the first report of a plant-derived carbon dot system that selectively engages and degrades ENO1, validating it as a druggable node in hepatic fibrosis.

Nevertheless, several questions warrant further investigation. Although we identified ENO1 as a primary target, the precise structural motifs on D-CDs responsible for this targeting remain to be deciphered. In addition, the long-term biodistribution, potential accumulation, and immune compatibility of repeatedly administered D-CDs require systematic evaluation. Future studies incorporating ENO1-knockout models or patient-derived HSCs could further validate the target and enhance the mechanistic credibility.

In conclusion, this study establishes a new strategy for treating hepatic fibrosis using an orally administered, plant-derived nano-degrader that targets ENO1. By fusing the targeted degradation paradigm with the translational advantages of herbal nanomedicine, our work provides a blueprint for developing mechanism-based, orally available therapeutics. Future efforts should focus on elucidating the precise surface moieties of D-CDs responsible for ENO1 recognition, evaluating long-term safety and

biodistribution, and validating this approach in patient-derived systems. This platform may also be extendable to other protein-driven fibrotic diseases, broadening its potential therapeutic impact.

Declarations

Ethics approval and consent to participate

All procedures involving animals were approved by the Animal Ethics Committee of Shandong First Medical University (No. W202410180680) and performed in compliance with institutional guidelines for the ethical use of laboratory animals.

Human liver tissue samples were obtained from patients with histopathologically confirmed hepatic fibrosis/cirrhosis as well as from control subjects with normal liver histology. All samples were collected with written informed consent from each participant and in strict accordance with the ethical guidelines approved by the Medical Ethics Committee of Zibo Central Hospital (Approval Number: 2026 YAN 025).

Author Contributions

Lin Gao, Teng Liu, Lin Gao, Yi-Kun Li, Ping Huang, Jing Li and Hong-Li Gao performed experiments, analyzed data, and participated in discussion of the results. Zhi-Yuan Lu, Jun-Xia Zheng, Teng Liu and Jing-Xin Li wrote and revised this manuscript. All authors have reviewed and approved the final version of the manuscript.

Acknowledgments

Not applicable.

Funding

This study was supported by grants from Shandong Provincial Natural Science Foundation (ZR2023ZD25, ZR2023QH427), Shandong Provincial Medical and Health Science and Technology Project (202513021296), Taishan Scholars Project in Shandong Province (tstp20230633, tsqn202408246) and the Joint Innovation Team for Clinical &Basic Research (202401).

Conflicts of Interest Statement

The authors declare no conflicts of interest.

Data Availability Statement

The data that support the findings of this study are available from the corresponding author upon reasonable request.

References

1. Taru V, Szabo G, Mehal W, Reiberger T. Inflammasomes in chronic liver disease: Hepatic injury, fibrosis progression and systemic inflammation. J Hepatol. 2024;81:895–910.
2. Hammerich L, Tacke F. Hepatic inflammatory responses in liver fibrosis. Nat Reviews Gastroenterol Hepatol. 2023;20:633–46.
3. Sharma S, Le Guillou D, Chen JY. Cellular stress in the pathogenesis of nonalcoholic steatohepatitis and liver fibrosis. Nat Reviews Gastroenterol Hepatol. 2023;20:662–78.
4. Friedman SL, Pinzani M. Hepatic fibrosis: 2022 Unmet needs and a blueprint for the future. Hepatology. 2022;75:473–88.
5. Rieder F, Nagy LE, Maher TM, Distler JHW, Kramann R, Hinz B, Prunotto M. Fibrosis: cross-organ biology and pathways to development of innovative drugs. Nat Rev Drug Discovery. 2025;24:543–69.
6. Di XP, Li Y, Wei JW, Li TY, Liao BH. Targeting Fibrosis: From Molecular Mechanisms to Advanced Therapies. Adv Sci 2025, 12.
7. Parola M, Pinzani M. Liver fibrosis in NAFLD/NASH: from pathophysiology towards diagnostic and therapeutic strategies. Mol Aspects Med 2024, 95.
8. Friedman SL, Neuschwander-Tetri BA, Rinella M, Sanyal AJ. Mechanisms of NAFLD development and therapeutic strategies. Nat Med. 2018;24:908–22.
9. Singh H, Razzaghi M, Ghorbanpoor H, Ebrahimi A, Avci H, Akbari M, Hassan S. Carbon dots in drug delivery and therapeutic applications. Adv Drug Deliv Rev. 2025;224:115644.
10. Zhong CL, Song NN, Huang P, Han LW, Zhang JG, Lu ZY, Wang L. Targeting Reactive Oxygen Species and Inflammation in Sepsis-Induced Liver Injury with Naturally Derived Superoxide Dismutase-Mimicking Carbon Dots. Biomaterials Res 2025, 29.
11. Wang L, Li ZY, Zhong CL, Teng ZY, Wang B, Rehman A, Han LW, Zeng KW, Zhang JG, Lu ZY. Therapeutic potential of naturally derived carbon dots in sepsis-associated acute kidney injury. Chin Med. 2025;20:49.
12. Lu Z, Li H, Song N, Wang Z, Wang H, Rehman A, Han L, Zeng K-W. Therapeutic Potential of Carbon Dots Derived from Phytochemicals as Nanozymes Exhibiting Superoxide Dismutase Activity for Anemia. ACS Appl Mater Interfaces. 2025;17:4562–78.
13. Liu Z-F, Wang J-H, Wang C-P, Wang Q, Li J, Han C-J, Lu Z-Y. Green hydrothermal valorization of Rosa damascena Mill. floral waste into functional carbon dots for anti-inflammatory nanomedicine. Ind Crops Prod. 2025;236:122115.
14. Liu FL, Zhang N, Wei M, Li YM, Liu XX, Han QY. A systematic review of the nano-technology applied in traditional Chinese medicines. Traditional Med Res. 2025;10:15.
15. Li H, Song N, Huang P, Li M, Wang Z, Han L, Liu T, Zeng K-W, Lu Z. Phytocarbon Nanodots Restore Glutathione Homeostasis via γ-Glutamylcysteine Synthetase against Ferroptosis-Driven Renal Fibrosis. *Authorea (preprint)* 2025.

16. Song N-N, Li H-J, Wang Y-Q, Kang X-Z, Gao L, Xie W, Han L-W, Yu M, Chen Z-K, Han B et al. 3D Structural Hijacking of Pathological α-Synuclein Fibrillar Architectures by Carbon Dot Nanoeraser Prevents Neurodegeneration. *Research Square (preprint)* 2025.
17. Liu Y, Zhang L, Cai H, Qu X, Chang J, Waterhouse GIN, Lu S. Biomass-derived carbon dots with pharmacological activity for biomedicine: Recent advances and future perspectives. Sci Bull. 2024;69:3127–49.
18. Liu Y, Wang D, Zheng WQ, Wang YX, Wang PY, Zhao YP, Liu XF, Shi YR, Wang Y, Zhou N, et al. Targeting JAK2 with a multifunctional nanoinhibitor for long-lasting anti-inflammatory effects and bone repair. J Nanobiotechnol. 2025;23:649.
19. Liu T, Wu Y, Wang C, Zhou TT, Yang RZ, Zhang X, Yan WL, Fan Q, Lu ZY. Mulberry-derived carbon dots attenuate kidney fibrosis through direct inhibition of PI3K. Mater Today Bio. 2025;35:102626.
20. Li L, Guo Y-D, Zhang X-W, Du Z-Y, Wang Y-Q, Yang Z, Luo Q-W, Zhuo F-F, Wei T-T, Liu Z-P, et al. Targeting G3BP1 Condensate Topology Promotes Stress Granule Assembly via m6A-IGF2BP1 for Ischemic Stroke Rescue. Adv Sci. 2026;13:e14703.
21. Lu ZY, Yu HZ, Li YX, Xu GS, Li XX, Liu YJ, Shen YM, Cai ZG, Zhao BB. Phosphatase, Mg2+/Mn2 + dependent 1B regulates the hematopoietic stem cell homeostasis via the Wnt/β-catenin signaling. Haematologica. 2024;109:2144–56.
22. Lu ZY, Huang LX, Li YX, Xu Y, Zhang RH, Zhou Q, Sun Q, Lu Y, Chen JJ, Shen YM, et al. Fine-Tuning of Cholesterol Homeostasis Controls Erythroid Differentiation. Adv Sci. 2022;9:2102669.
23. Guo MX, Zhao HX, Song NN, Huang P, Li M, Han LW, Zeng KW, Lu ZY. Shenmai injection attenuates sepsis-associated acute lung injury by remodeling gut microbiota and restoring steroid hormone biosynthesis. Fitoterapia. 2025;187:106935.
24. Boukhvalov DW, Osipov VY, Murzalinov D, Serikkanov A, Bi H. A comprehensive model of carbon nanodots with 0.21 nm lattice fringes patterns. Carbon. 2024;225:119101.
25. Yao L, Zhao MM, Luo QW, Zhang YC, Liu TT, Yang Z, Liao M, Tu PF, Zeng KW. Carbon Quantum Dots-Based Nanozyme from Coffee Induces Cancer Cell Ferroptosis to Activate Antitumor Immunity. ACS Nano. 2022;16:9228–39.
26. Higashi T, Friedman SL, Hoshida Y. Hepatic stellate cells as key target in liver fibrosis. Adv Drug Deliv Rev. 2017;121:27–42.
27. Kim KK, Sheppard D, Chapman HA. TGF-β1 Signaling and Tissue Fibrosis. Cold Spring Harb Perspect Biol. 2018;10:a022293.
28. Lu HL, Huang J, Wang YC, Casals E, Casals G, Zeng ML. Beyond M1/M2: The role of reactive oxygen species in liver fibrosis and immune modulation. Redox Biol. 2025;88:103933.
29. Innocenzi P, Stagi L. Carbon dots as oxidant-antioxidant nanomaterials, understanding the structure-properties relationship. A critical review. Nano Today. 2023;50:101837.
30. Runyan CE, Schnaper HW, Poncelet AC. The phosphatidylinositol 3-kinase/Akt pathway enhances Smad3-stimulated mesangial cell collagen I expression in response to transforming growth factor-β1. J Biol Chem. 2004;279:2632–9.

31. Sun L, Suo C, Zhang T, Shen S, Gu X, Qiu S, Zhang P, Wei H, Ma W, Yan R, et al. ENO1 promotes liver carcinogenesis through YAP1-dependent arachidonic acid metabolism. Nat Chem Biol. 2023;19:1492–503.
32. Shi Y, Liu J, Zhang R, Zhang M, Cui H, Wang L, Cui Y, Wang W, Sun Y, Wang C. Targeting Endothelial ENO1 (Alpha-Enolase) -PI3K-Akt-mTOR Axis Alleviates Hypoxic Pulmonary Hypertension. Hypertension. 2023;80:1035–47.
33. Sun N, Wang YB, Huang J, Deng RW, He HY, Gao L, Gao X, Fan YL, Cong Y, Guo YL, et al. Irisin Attenuates Pulmonary Vascular Remodeling in Pulmonary Arterial Hypertension via Ubiquitin-Mediated Regulation of ENO1. Adv Sci. 2025;12:202500096.
34. Zhang WY, Gao J, Shen FK, Ma XY, Wang ZH, Hou XT, Hao EW, Hou YY, Bai G. Cinnamaldehyde changes the dynamic balance of glucose metabolism by targeting ENO1. Life Sci. 2020;258:118151.
35. Watson BR, Paul B, Rahman RU, Amir-Zilberstein L, Segerstolpe A, Epstein ET, Murphy S, Geistlinger L, Lee T, Shih A, et al. Spatial transcriptomics of healthy and fibrotic human liver at single-cell resolution. Nat Commun. 2025;16:319.
36. Bao YL, Wang L, Pan HT, Zhang TR, Chen YH, Xu SJ, Mao XL, Li SW. Animal and Organoid Models of Liver Fibrosis. Front Physiol. 2021;12:666138.
37. Fang KL, Qi XY, Han QT, Chen LZ, Wang XN, Xu ZP, Shang LQ, Shen T. Protective effect of lycorine hydrochloride against diabetic nephropathy in high-fat diet and streptozotocin-induced diabetic mice. Pharm Sci Adv. 2024;2:100035.
38. Mok ZH. The effect of particle size on drug bioavailability in various parts of the body. Pharm Sci Adv. 2024;2:100031.
39. Schuppan D, Surabattula R, Wang XY. Determinants of fibrosis progression and regression in NASH. J Hepatol. 2018;68:238–50.
40. Liu L, Guan X, Zhuo J, Wu X, Han X. PROTACs improve selectivity for targeted proteins. Acta Materia Med. 2025;4:390–412.
41. Teja PK, Mithiya J, Kate AS, Bairwa K, Chauthe SK. Herbal nanomedicines: Recent advancements, challenges, opportunities and regulatory overview. Phytomedicine. 2022;96:153890.
42. Kumari S, Malla R. New Insight on the Role of Plasminogen Receptor in Cancer Progression. Cancer Growth Metastasis. 2015;8:35–42.

Scheme 1

Scheme 1 is available in the Supplementary Files section.

Figures

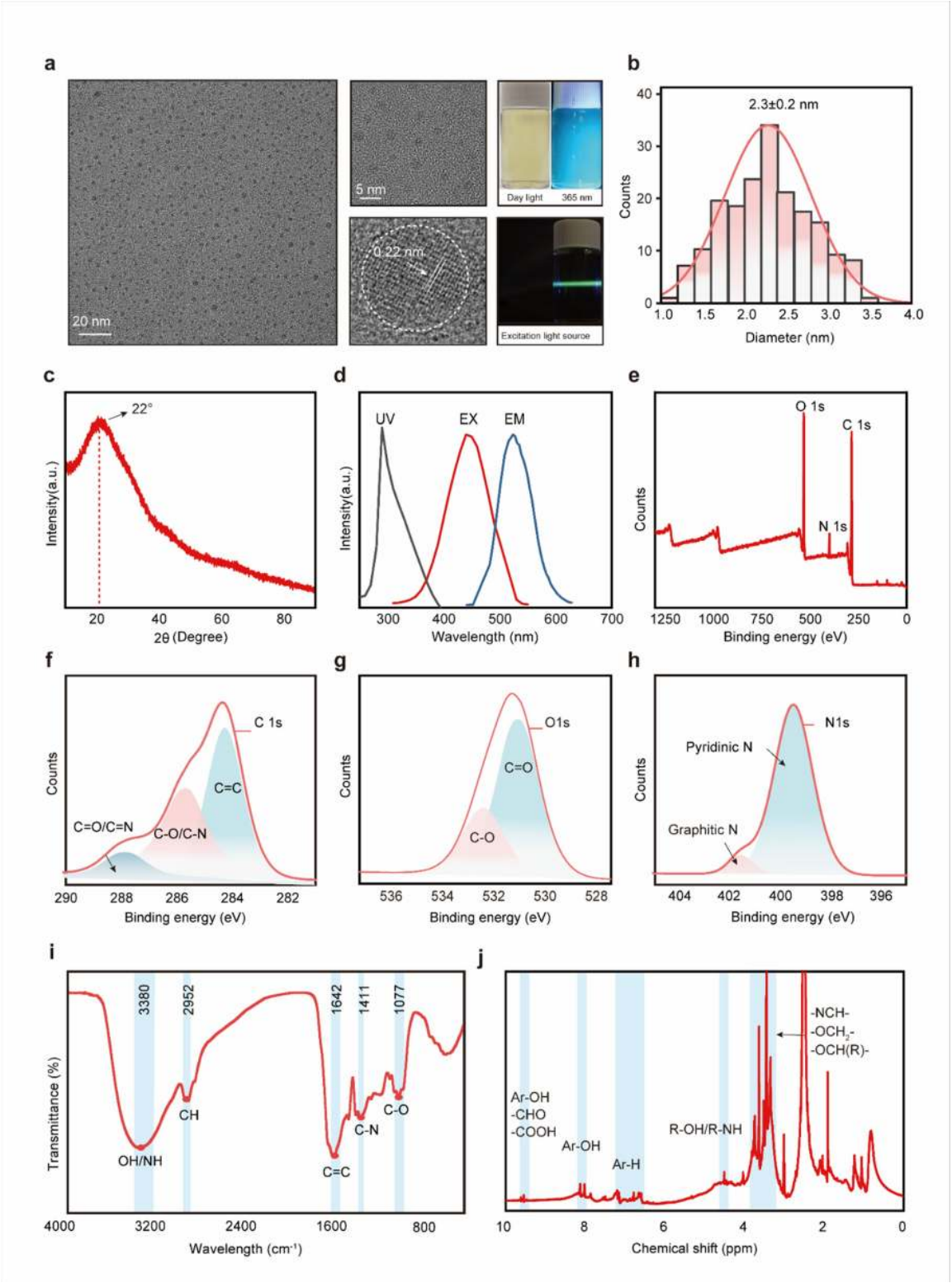

Figure 1

Characterization of D-CDs. (a) TEM image (insets: size distribution, lattice fringes, and D-CDs solution under white-light and 365 nm UV illumination). (b) Particle-size distribution. (c) XRD pattern. (d) UV-vis absorption (black), excitation (red), and emission (blue) spectra. (e) XPS survey spectrum. (f) C 1s, (g) O 1s, (h) N 1s high-resolution spectra. (i) FT-IR spectra. (j) ^{1}H NMR spectrum of D-CDs.

In summary, comprehensive characterization encompassing morphology, optical properties, environmental stability, surface chemistry, and molecular structure demonstrates that D-CDs possess a well-defined quasi-spherical nanostructure, establishing them as a promising theranostic platform for targeted biomedical applications.

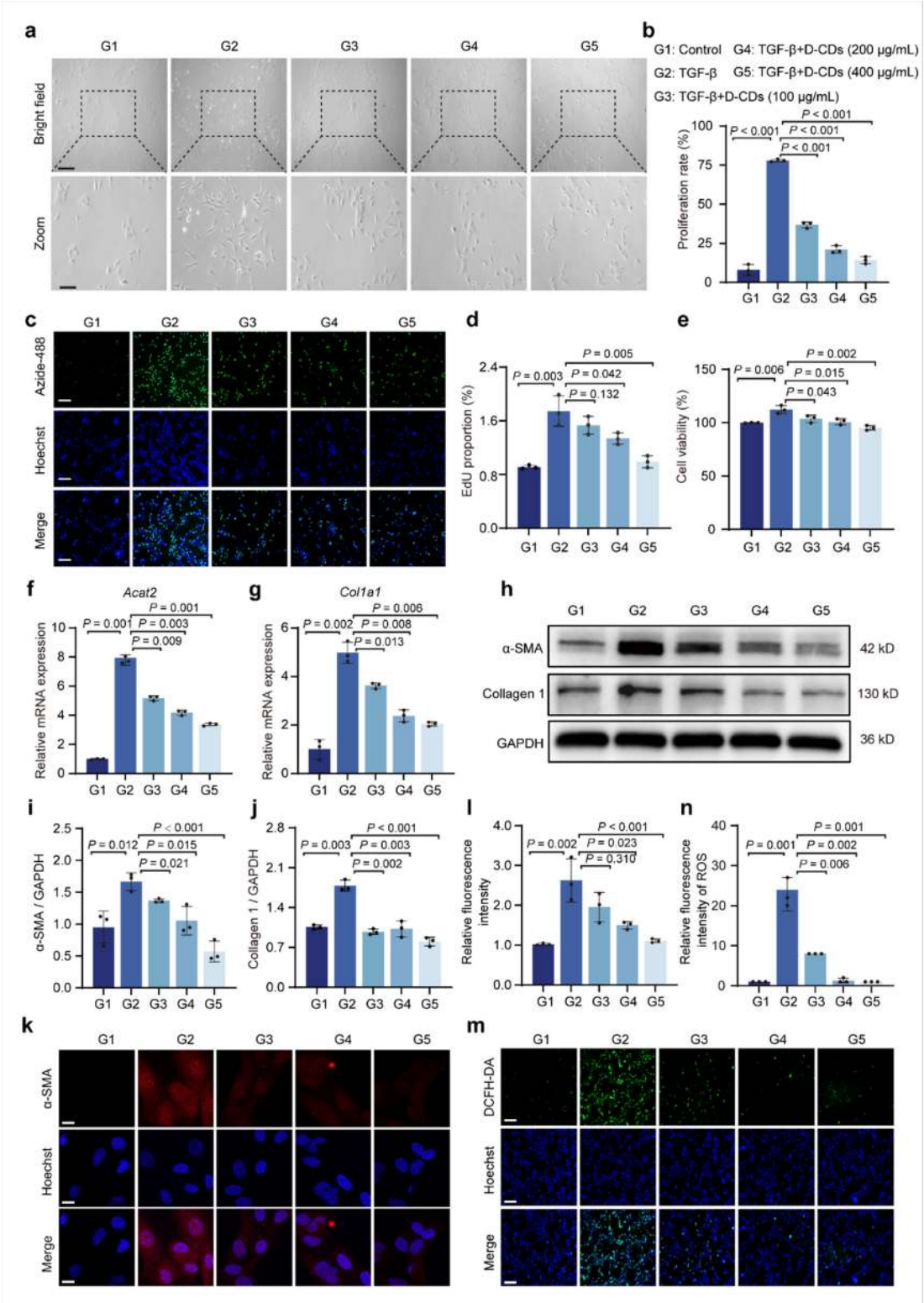

Figure 2

D-CDs ameliorate TGF-β–induced fibrotic activation in LX-2 cells *in vitro*. (a) Bright-field images showing morphological changes of LX-2 cells after 4 days of TGF-β stimulation with or without D-CDs treatment. Scale bar: 100 μm. (b) Quantification of cell proliferation based on bright-field image analysis. (c, d) EdU assay evaluating cell proliferation: (c) representative images and (d) corresponding statistical analysis. Scale bar: 100 μm. (e) Cell proliferation measured by CCK-8 assay under indicated treatments. (f, g) mRNA expression levels of α-SMA and Collagen 1 were analyzed by RT-qPCR. (h) Western blot analysis of α-SMA and Collagen 1 protein expression. (I, j) Quantification of α-SMA (i) and Collagen 1 (j) protein levels from Western blot data. (k) Representative immunofluorescence images of α-SMA (green) in LX-2 cells. Scale bar: 10 μm. (l) Quantitative analysis of α-SMA fluorescence intensity. (m) Representative fluorescence micrographs showing intracellular ROS levels detected by DCFH-DA probe. Scale bar: 100 μm. (n) Quantitative analysis of intracellular ROS levels corresponding to (m). Data represent mean ± SD (n = 3). Statistical significance was calculated by using an unpaired two-tailed Student’s t-test.

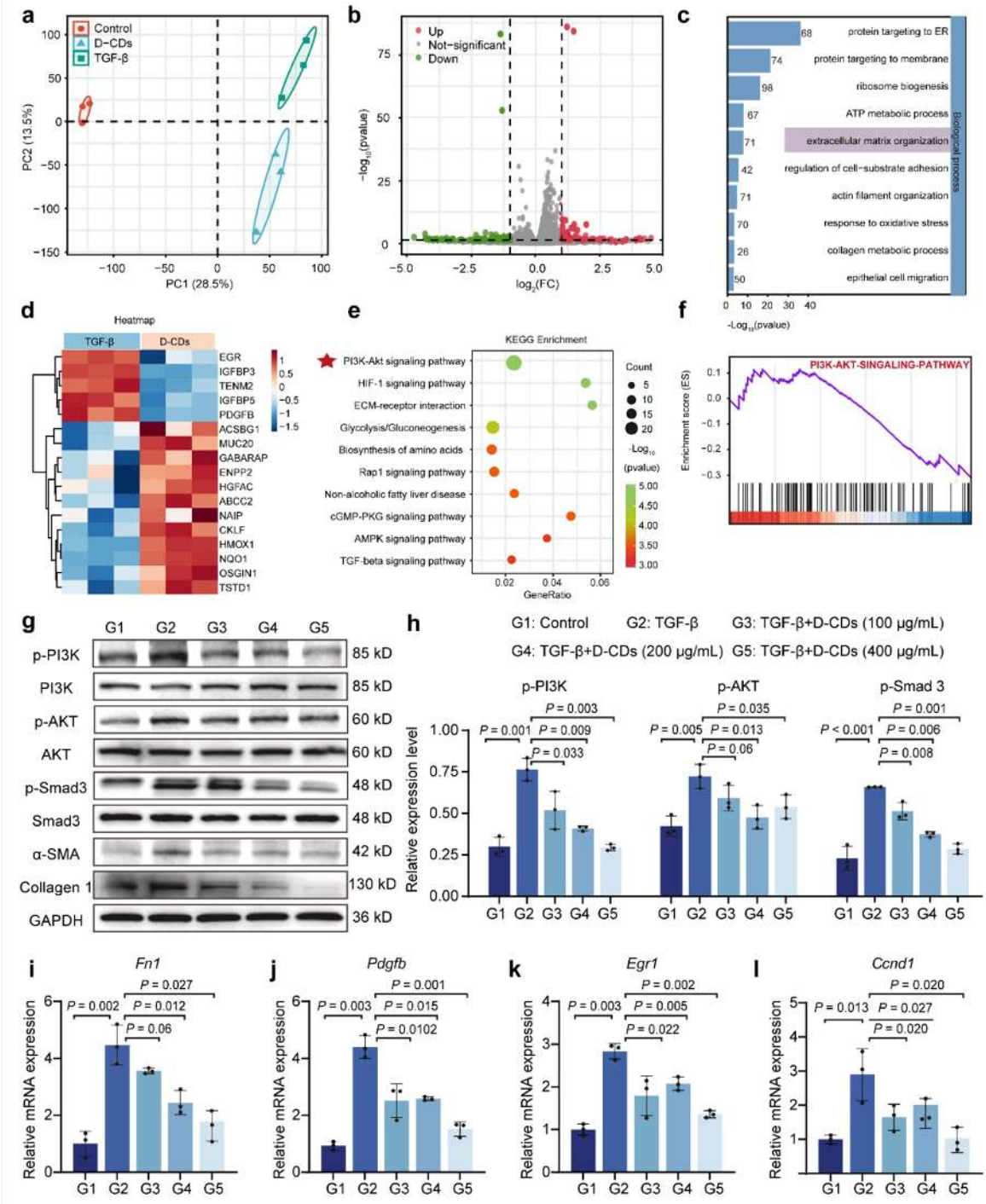

Figure 3

D-CDs alleviate hepatic fibrosis through suppression of the PI3K/AKT signaling pathway. (a) PCA of transcriptomic profiles from control, model (TGF-β-treated), and D-CDs-treated LX-2 cells. (b) Volcano plot showing differentially expressed genes between the model and D-CD-treated groups. (c) GO enrichment analysis of up-regulated biological processes. (d) Heatmap of fibrosis-related gene expression from RNA-seq data. (e) KEGG pathway enrichment analysis of differentially expressed genes.

(f) GSEA result showing inhibition of the PI3K/AKT signaling pathway after D-CD treatment. (g) Western blot analysis of key proteins in the PI3K/AKT and Smad pathways. (h) Quantification of p-PI3K, p-AKT, and p-Smad3 protein levels from three independent experiments. (i-l) mRNA expression levels of *Fn1*, *Pdgfb*, and *Ccnd1* analyzed by RT-qPCR. Data represent mean ± SD (n = 3). Statistical significance was calculated by using an unpaired two-tailed Student's t-test.

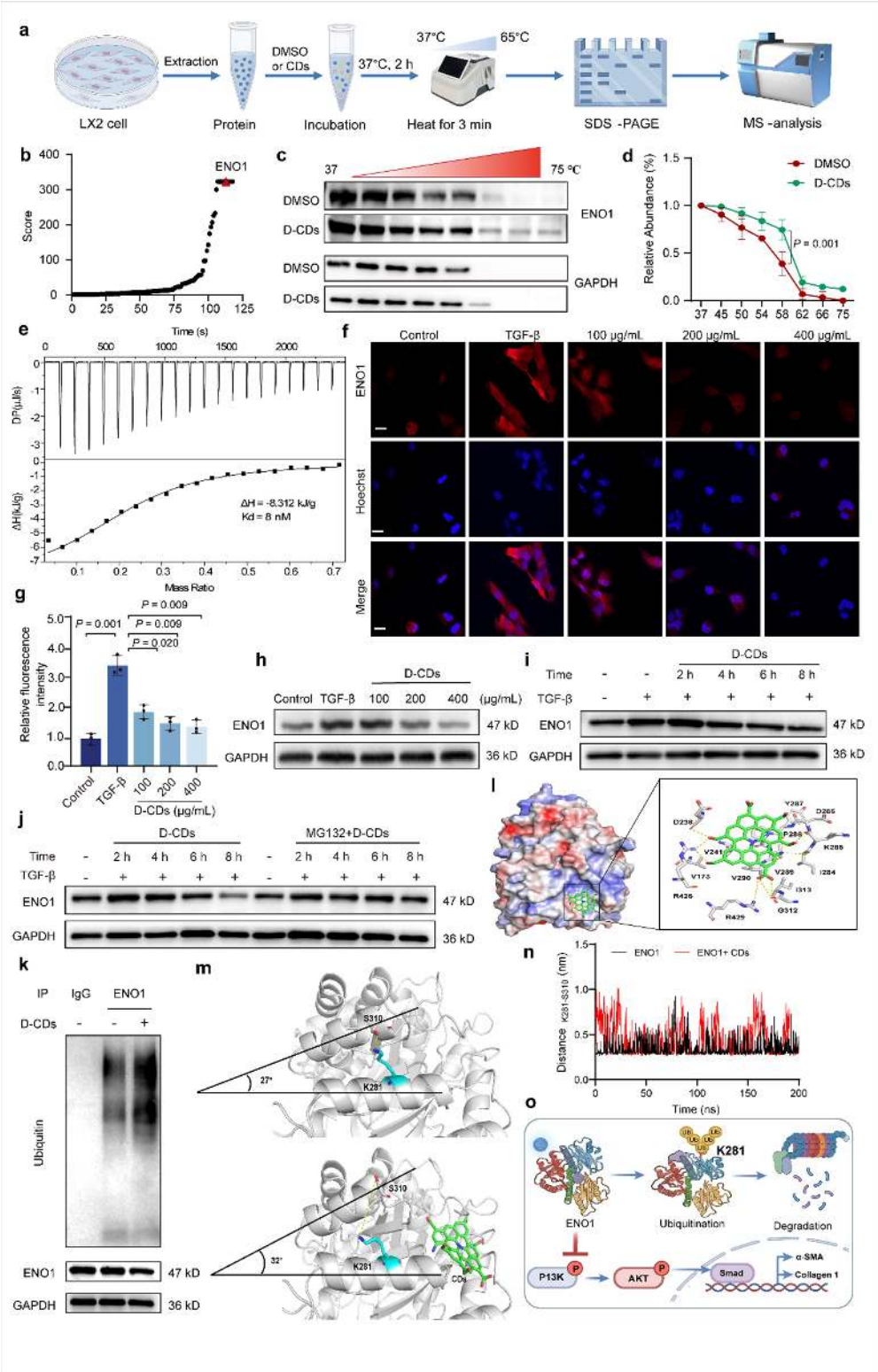

Figure 4

D-CDs target ENO1 for ubiquitin-proteasome degradation via an allosteric mechanism. (a) Cellular thermal shift assay (CETSA) workflow. (b) Protein binding affinity scores of D-CDs. (c) CETSA evaluation of the binding between D-CDs and ENO1. (d) Quantitative analysis of ENO1 thermal stability. (e) ITC analysis of D-CDs binding to ENO1. (f) Immunofluorescence staining of ENO1 (red) in LX-2 cells. Scale bar: 10 μm. (g) Quantitative analysis of ENO1 fluorescence intensity. (h) Western blot analysis of ENO1 protein expression after D-CDs treatment. (i) Time-dependent degradation of ENO1 protein following D-CDs exposure. (j) ENO1 protein expression with or without the proteasome inhibitor MG132 after D-CDs treatment. (k) Analysis of ENO1 ubiquitination levels. (l) Binding pose of D-CDs (green) at a surface cavity of ENO1, with key interacting residues shown as sticks. Hydrogen bonds and hydrophobic interactions are indicated by dashed lines. (m) Conformational change induced by D-CDs binding, showing increased distance and angle between α-helix 7 and α-helix 8. (n) Enhanced solvent exposure of the ubiquitination site K281 due to disrupted packing with S310. (o) Schematic illustration of the allosteric degradation mechanism of ENO1 by D-CDs. Data represent mean ± SD (n = 3). Statistical significance was calculated by using an unpaired two-tailed Student’s t-test.

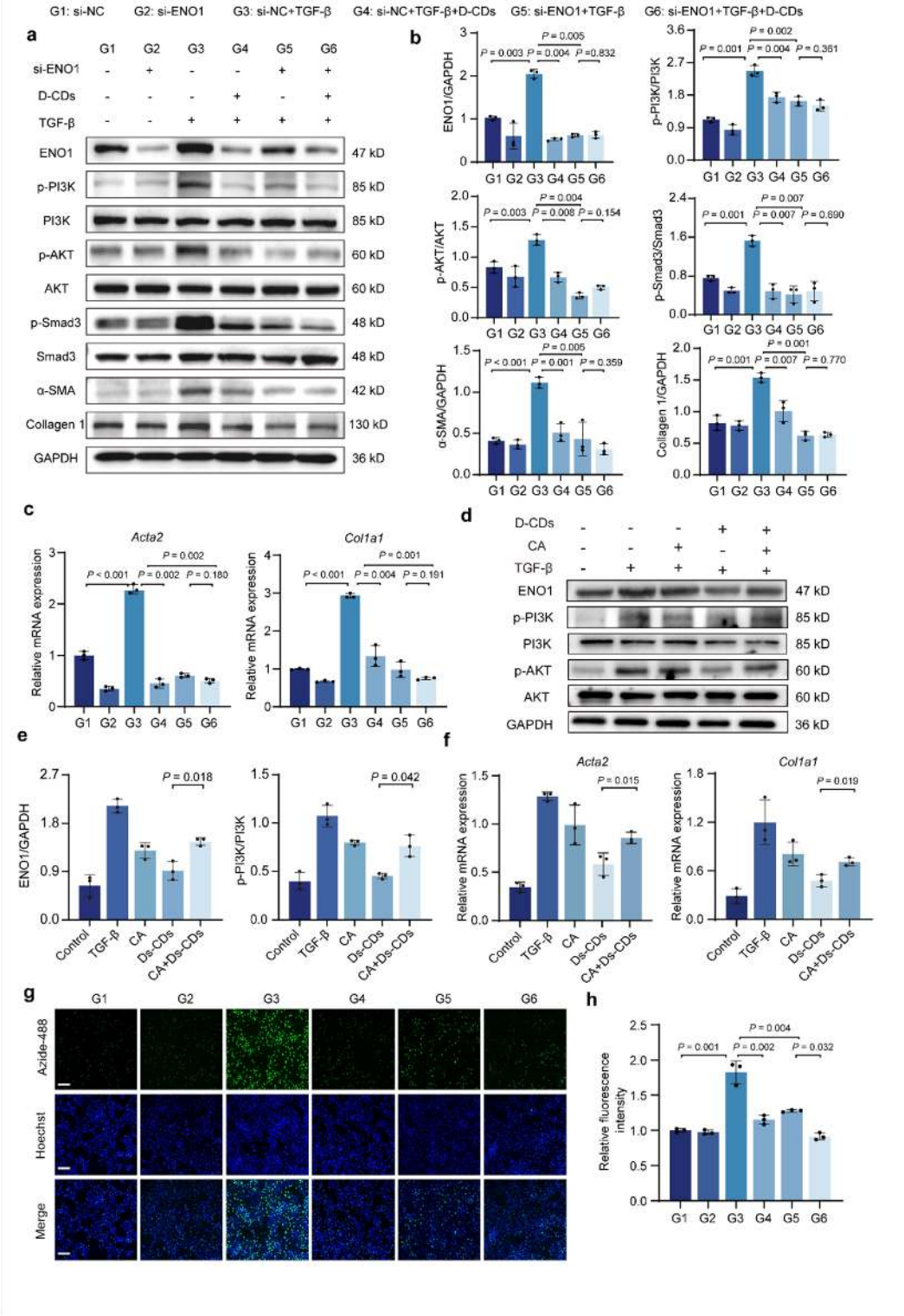

Figure 5

The anti-fibrotic effect of D-CDs is ENO1-dependent. (a) Western blot analysis of ENO1, downstream signaling proteins (p-PI3K, p-AKT, p-Smad3), and fibrotic markers (α-SMA, collagen I) after TGF-β stimulation. (b) Quantitative analysis of the protein levels shown in (a). (c) mRNA expression levels of Acta2 (α-SMA) and Col1a1 (collagen I) in control and ENO1-knockdown cells, measured by RT-qPCR. (d) Western blot showing that co-treatment with CA reverses the D-CDs-mediated reduction of ENO1 protein

and restores the phosphorylation of PI3K and AKT. (e) Quantification of protein levels from (d). (f) mRNA expression of Acta2 and Col1a1 after treatment with D-CDs, CA, or their combination, analyzed by RT-qPCR (n = 3). (g) Representative images of EdU staining (green) in control and ENO1-knockdown LX-2 cells under TGF-β stimulation. Nuclei were counterstained with DAPI (blue). (h) Quantitative analysis of EdU-positive cells. Statistical significance was calculated by using an unpaired two-tailed Student's t-test. All quantitative data, derived from three biologically independent replicates, are shown as mean ± SD.

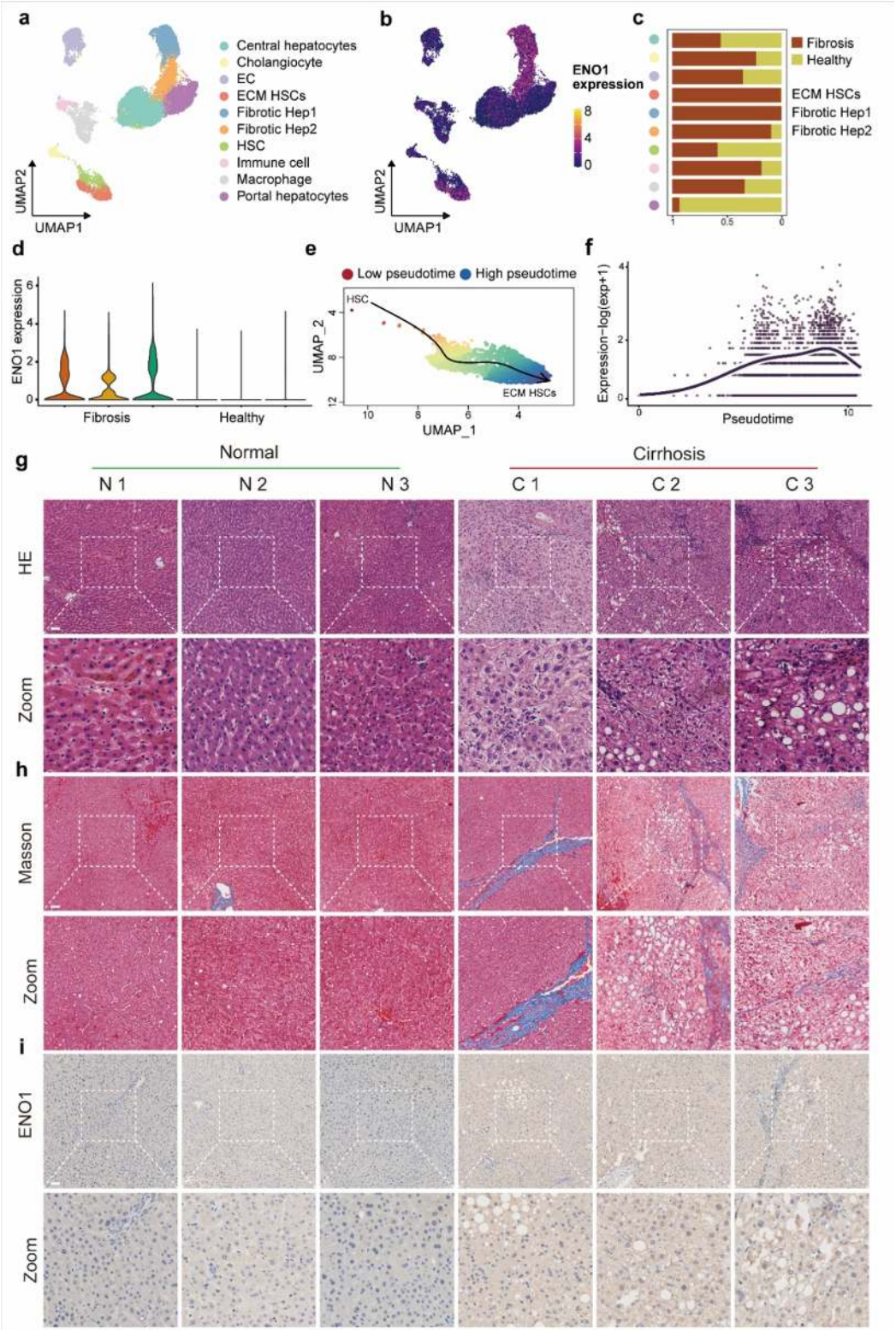

Figure 6

Single-cell and histopathological validation of ENO1 as a fibrosis-associated target in human liver. (a) UMAP visualization of integrated scRNA-seq data from fibrotic and healthy human livers. (b) ENO1 expression across cell types visualized in a feature plot. (c) Cell-type proportions in fibrotic versus healthy livers. (d) Violin plot comparing overall ENO1 expression between fibrotic and control tissues. (e) Pseudotime trajectory (Slingshot) illustrating HSC differentiation toward ECM HSCs. (f) ENO1 expression dynamics along pseudotime. (g) Representative H&E staining of human liver sections. (h) Masson's trichrome staining highlighting collagen deposition (blue) in fibrotic septa. (i) Immunohistochemical staining for ENO1. Scale bars: 100 μm (g-i).

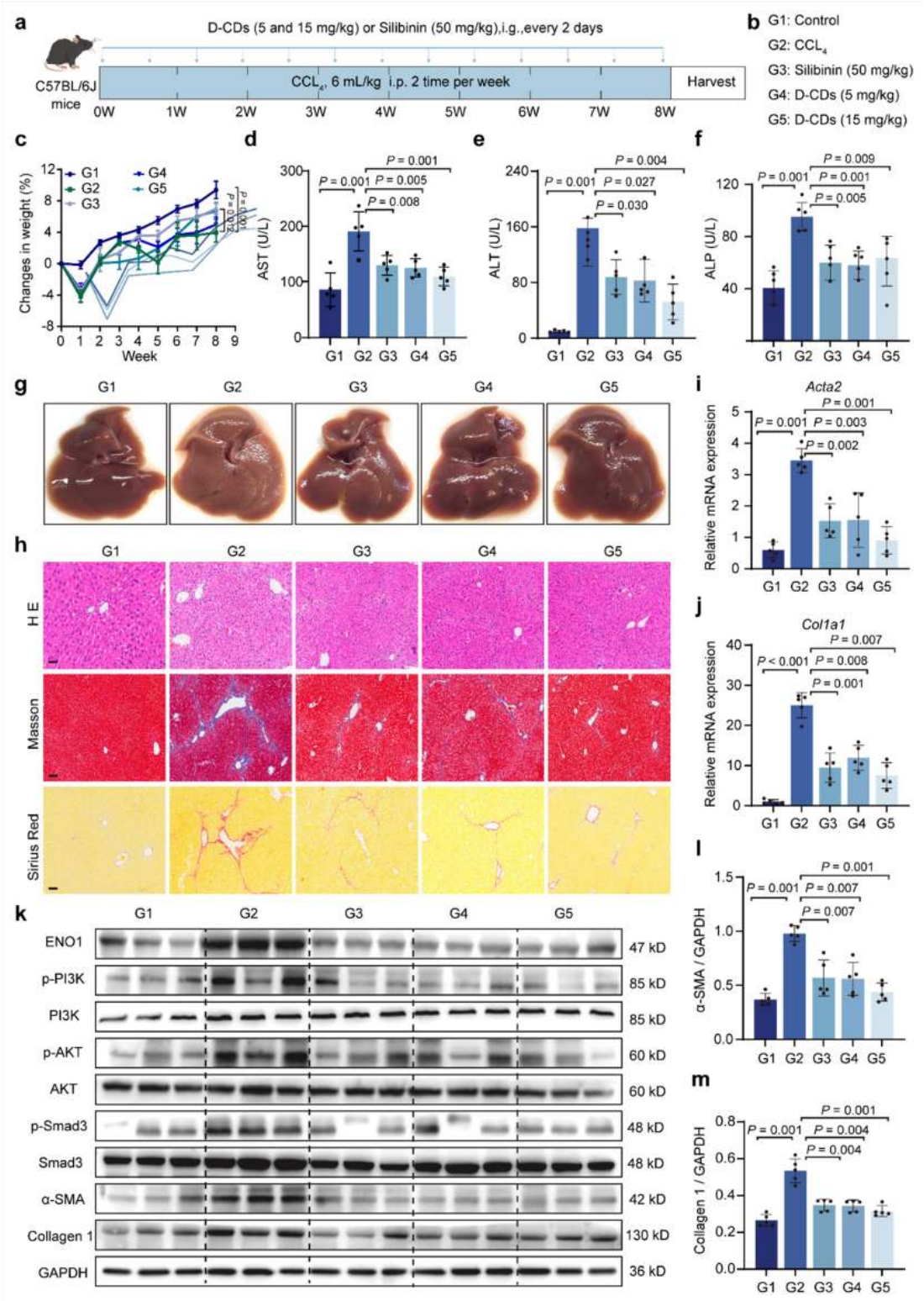

Figure 7

Therapeutic efficacy of D-CDs in CCl_4-induced hepatic fibrosis in mice. (a) Schematic of the CCl_4-induced fibrosis model and oral D-CDs treatment regimen. (b) List of experimental groups. (c) Changes in mouse body weight during the treatment period (n = 8). (d-f) Serum levels of aspartate aminotransferase (AST), alanine aminotransferase (ALT) and alkaline phosphatase (ALP) across experimental groups (n = 5). (g) Representative macroscopic images of livers from each group. (h) Representative histopathological

images of liver sections stained with H&E, Sirius Red, and Masson's trichrome (n = 5, Scale bar: 100 μm). (I, j) Hepatic mRNA expression levels of α-SMA (i) and Collagen 1 (j) measured by RT-qPCR (n = 5). (k) Western blot analysis of indicated proteins in liver lysates (n = 5). (l, m) Quantitative analysis of α-SMA (l) and Collagen 1 (m) protein levels (n = 5). Data represent mean ± SD. Statistical significance was calculated by using an unpaired two-tailed Student's t-test.

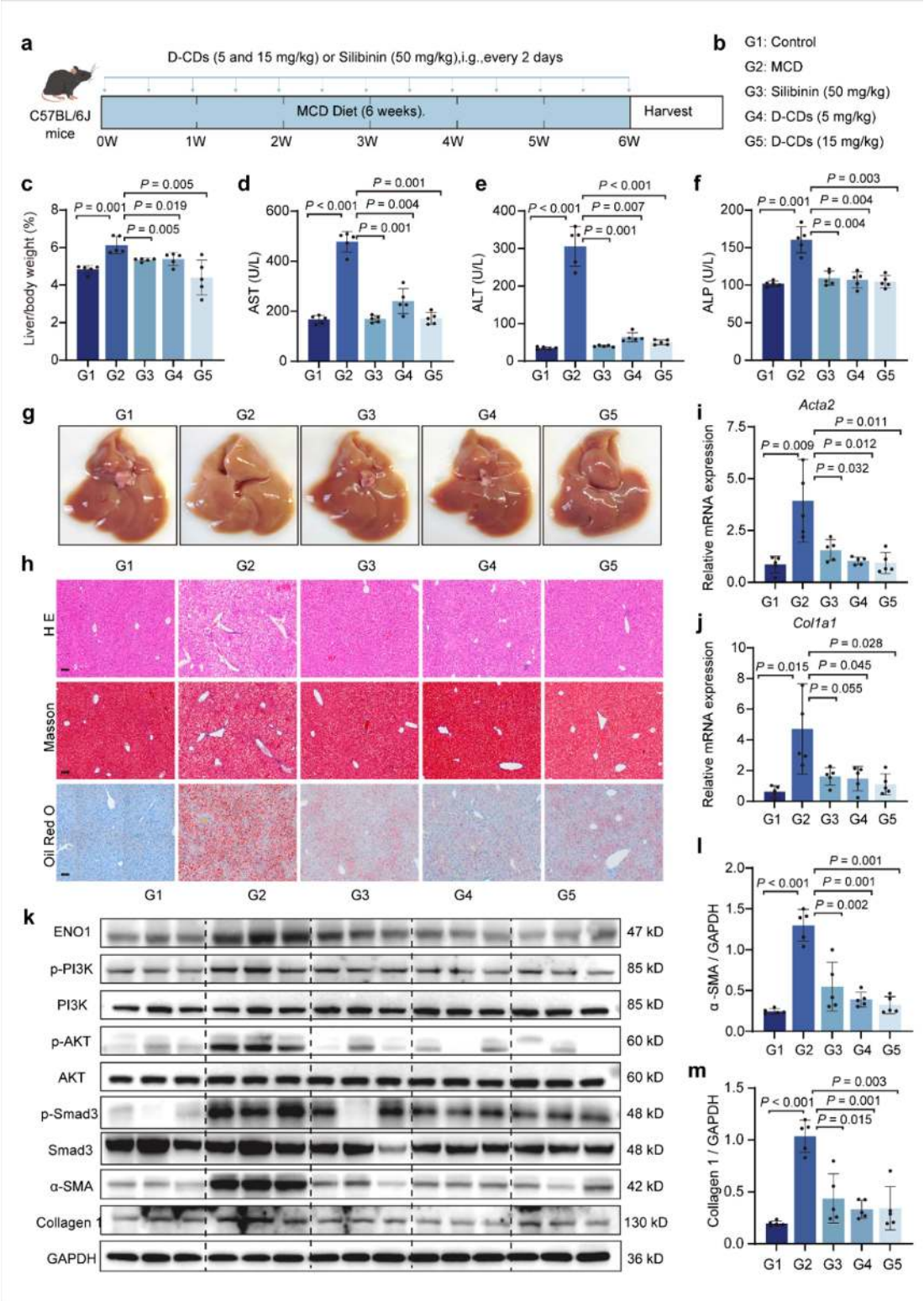

Figure 8

D-CDs attenuate MCD diet-induced hepatic fibrosis in mice. (a) Schematic of the MCD diet-induced fibrosis model and D-CDs treatment timeline. (b) List of experimental groups. (c) Liver-to-body weight ratio in mice (n = 8). (d-f) Serum levels of AST, ALT and ALP across experimental groups (n = 5). (g) Representative macroscopic images of livers from each group. (h) Representative histopathological images of liver sections stained with H&E, Sirius Red, and Masson's trichrome (n = 5, Scale bar: 100 μm). (I, j) Hepatic mRNA expression levels of α-SMA (i) and Collagen 1 (j) measured by RT-qPCR (n = 5). (k) Western blot analysis of indicated proteins in liver lysates (n = 5). (l, m) Quantitative analysis of α-SMA (l) and Collagen 1 (m) protein levels (n = 5). Data represent mean ± SD. Statistical significance was calculated by using an unpaired two-tailed Student's t-test.

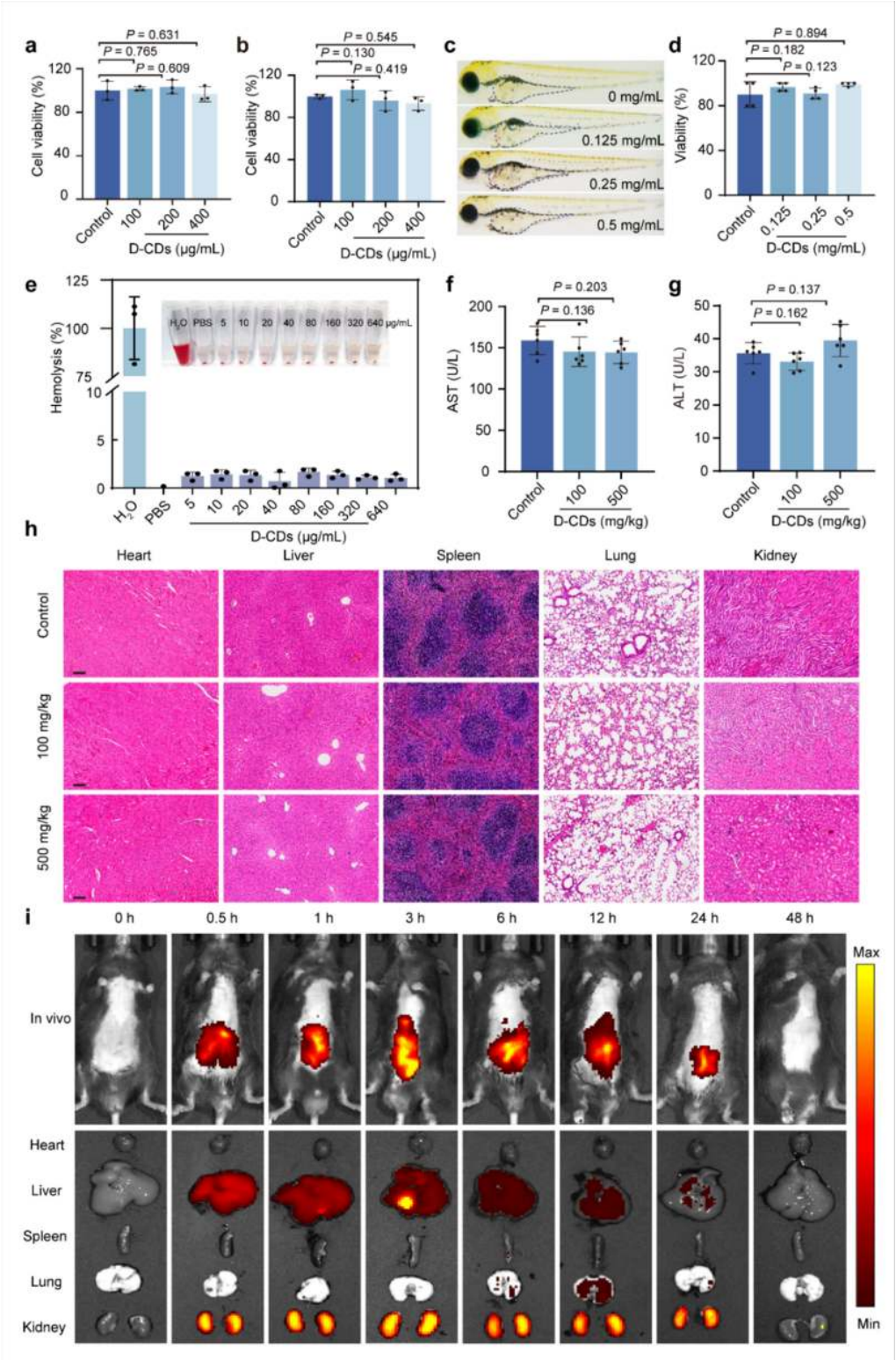

Figure 9

Biosafety and biodistribution profile of D-CDs. (a, b) Viability of (a) AML-12 and (b) HUVEC cells after 24 h incubation with increasing concentrations of D-CDs. (c) Representative bright-field images of zebrafish following exposure to D-CDs. (d) Survival rates of zebrafish post-fertilization following treatment with indicated concentrations of D-CDs. Each dot represents ten zebrafish embryos. (e) Hemolysis assay of D-CDs. (n = 3). (f, g) Serum levels of AST and ALT across different treatment groups. (n = 6) (h)

Hematoxylin and eosin (H&E) staining of major organs from mice in different groups. (n = 4) (i) *In vivo* fluorescence imaging of mice at different time points after intravenous injection of Cy5-labeled D-CDs (D-CDs@Cy5) (n = 3). Quantification of overall fluorescence intensity is shown in the adjacent panel. Data represent mean ± SD. Statistical significance was calculated by using an unpaired two-tailed Student's t-test.

Supplementary Files

This is a list of supplementary files associated with this preprint. Click to download.

- SupplementalInformation.docx
- floatimage1.jpeg